

# Poisson Log-Normal Process for Count Data Prediction

Anushka Saha,<sup>1</sup> Abhijith Gandrakota,<sup>2</sup> and Alexandre V. Morozov<sup>1,\*</sup>

<sup>1</sup>*Department of Physics & Astronomy, Rutgers, The State University of New Jersey,  
136 Frelinghuysen Rd., Piscataway, NJ 08854, U.S.A.*

<sup>2</sup>*Fermi National Accelerator Laboratory, Batavia, IL 60510, U.S.A.*

Modeling count data is important in physics and other scientific disciplines, where measurements often involve discrete, non-negative quantities such as photon or neutrino detection events. Traditional parametric approaches can be trained to generate integer-count predictions but may struggle with capturing complex, non-linear dependencies often observed in the data. Gaussian process (GP) regression provides a robust non-parametric alternative to modeling continuous data; however, it cannot generate integer outputs. We propose the Poisson Log-Normal (PoLoN) process, a framework that employs GP to model Poisson log-rates. As in GP regression, our approach relies on the correlations between data points captured via GP kernel structure rather than explicit functional parameterizations. We demonstrate that the PoLoN predictive distribution is Poisson-LogNormal and provide an algorithm for optimizing kernel hyperparameters. Furthermore, we adapt the PoLoN approach to the problem of detecting weak localized signals superimposed on a smoothly varying background – a task of considerable interest in many areas of science and engineering. Our framework allows us to predict the strength, location and width of the detected signals. We evaluate PoLoN’s performance using both synthetic and real-world datasets, including the open dataset from CERN which was used to detect the Higgs boson at the Large Hadron Collider. Our results indicate that the PoLoN process can be used as a non-parametric alternative for analyzing, predicting, and extracting signals from integer-valued data.

## I Introduction

In a wide range of scientific disciplines, including experimental particle physics, materials science, chemistry, and astrophysics, measurements naturally come in the form of non-negative integer counts. The counts are reported as a function of one or several variables such as energy, wavelength, frequency, or time. For example, in the Higgs boson search at the Large Hadron Collider (LHC), the data represents the number of di-photon events per energy bin [1, 2], where energy refers to the invariant mass of the di-photon system,  $m_{\gamma\gamma}$ . In electron energy loss spectroscopy (EELS), raw data consists of the number of electrons detected per energy-loss bin as a high-energy electron beam passes through a thin sample and electrons scatter inelastically [3, 4]. In X-ray photoelectron spectroscopy (XPS), the number of photoelectrons is reported as a function of binding energy as X-ray photons eject core electrons from the sample [5–7]. In neutrino detection, the data is often presented as the number of neutrino detection events as a function of the neutrino energy or the angular sky map, which keeps track of neutrino arrival directions [8–11]. In astrophysics, photoelectron or photon counts, measured as a function of time, appear in the context of exoplanet searches (detection of small periodic dips in transient light curves) [12, 13] as well as optical/UV [14, 15] or high-energy (gamma-ray, X-ray) [16, 17] transient detection.

Thus, there is a substantial need in the scientific community to develop machine learning methods capable of assigning probabilities directly to integer counts. Such models should be able to make non-trivial generalizations, for example predicting the number of events for time intervals or energy bins where no training data is available. Ideally, these models would also provide a quantitative measure of prediction uncertainty, which could be used to estimate statistical significance of various signals. An important application of such an approach is de-noising – constructing a smoothly varying prediction on the basis of a limited number of noisy observations [18, 19].

In the above examples and many others, a key data analysis task is to separate a smooth, slowly varying background from relatively sharp, localized signals. Numerous algorithms for signal-background decomposition (also known as background modeling or removal) have been developed in the literature, including asymmetric least squares (ALS) and its variants (arPLS/airPLS) [20], Poisson wavelet denoising and background modeling [18], and explicit background modeling with Bernstein or polynomial fits [2]. These methods do not respect the integer count nature of the data however, which may become important in the regions where the number of observed events is close to zero.

Traditional approaches to modeling integer count data include Poisson and negative binomial regression [21–24]. These methods employ parametric regression and maximum likelihood estimation and therefore depend on a heuristic

---

\* [morozov@physics.rutgers.edu](mailto:morozov@physics.rutgers.edu)

choice of input features, requiring careful feature selection to balance model flexibility against the risk of overfitting [25, 26]. As a nonparametric alternative, Gaussian Process (GP) regression offers a Bayesian framework that is well-suited for modeling smooth functions and quantifying predictive uncertainty [27–29]. GP regression is defined in terms of kernel functions, which specify the degree of correlation between two points in the dataset [27, 28]. GP regression techniques have been recently applied to diverse fields such as astrophysics [30–33], gravitational wave detection [34], and high-energy particle physics [19, 35]. However, standard GP regression is not directly applicable to integer-valued data since it assumes Gaussian likelihoods of continuous outputs.

To address this limitation, we propose the Poisson Log-Normal process (PoLoN), a novel modeling framework that enables a principled application of Gaussian processes to non-negative integer count data. Specifically, we model Poisson log-rates as a Gaussian process; exponentiation of these log-rates ensures positivity of the Poisson rates themselves. We show that the integer-valued PoLoN predictive distribution is given by the Poisson-LogNormal (PLN) distribution [36, 37]. Similar to the standard GP regression, the PLN predictive distribution provides both the best model (through the mean or the mode of the predictive distribution) and a measure of its uncertainty (through the variance of the predictive distribution).

We demonstrate the predictive power of the PoLoN framework on a number of synthetic and real-world datasets. We focus in particular on the task of detecting localized signals superimposed on the smoothly varying background, modifying the PoLoN procedure to build an explicit functional representation of the signal into the Poisson rates (we refer to this signal-background decomposition approach as PoLoN-SB). As a result, we are able to efficiently estimate the parameters of the signal, reconstruct its shape, and estimate its statistical significance with respect to the background distribution. Our approach is applicable to any situation in which observations consist of event counts, including numerous setups which require robust decomposition of the observed count data into signal and background components.

## II Materials and Methods

### A Predictive distribution

Let us consider a training dataset  $D = \{(\vec{X}_n, t_n)\}_{n=1}^N$ , where  $\vec{X}_n$  are input feature vectors and  $t_n$  are non-negative integer target variables. We assume that the observed integer counts  $\{t_n\}$  are Poisson-distributed with rate parameters  $\{\alpha(\vec{X}_n)\}$ . To ensure the positivity of Poisson rates, we express them as  $\alpha(\vec{X}_n) = e^{\lambda(\vec{X}_n)}$ . Then the probability of a target integer  $t$  is given by

$$p(t|\lambda) = \frac{e^{t\lambda} e^{-e^\lambda}}{t!}, \quad t = 0, 1, 2, \dots. \quad (1)$$

Let  $t_{N+1}$  denote a new target variable corresponding to an input feature vector  $\vec{X}_{N+1}$ ;  $(\vec{X}_{N+1}, t_{N+1})$  is not included in the training set. We assume that the new target variable is also Poisson distributed with the log-rate  $\lambda(\vec{X}_{N+1})$ . Our objective is to determine the predictive distribution  $p(t_{N+1}|\vec{t}_N)$ , where  $\vec{t}_N = [t_1 \dots t_N]^T$  is a vector of target variables in the training set (we omit the conditional dependence on  $\{\vec{X}_n\}_{n=1}^N$  for brevity).

We define a vector  $\vec{\lambda}_{N+1} = [\lambda(\vec{X}_1) \dots \lambda(\vec{X}_{N+1})]^T$  which comprises Poisson log-rates for all  $N+1$  datapoints. We assume that  $\vec{\lambda}_{N+1}$  is generated by the Gaussian process [27, 28]: the joint probability of  $\vec{\lambda}_{N+1}$  is given by the multivariate Gaussian distribution:

$$p(\vec{\lambda}_{N+1}) = \mathcal{N}(\vec{\lambda}_{N+1}|\vec{0}, C_{N+1}), \quad (2)$$

where  $\vec{0}_{N+1}$  is a null vector of size  $N+1$  and the  $(n, m)$  element of the  $(N+1) \times (N+1)$  covariance matrix  $C_{N+1}$  is given by

$$C_{N+1,nm} = C_{N+1}(\vec{X}_n, \vec{X}_m) = k_{\vec{\theta}}(\vec{X}_n, \vec{X}_m) + \epsilon \delta_{nm}, \quad (3)$$

where  $k_{\vec{\theta}}(\vec{X}, \vec{Y})$  is a pre-specified kernel function with the hyperparameters  $\vec{\theta}$ ,  $\epsilon > 0$  is a small positive constant added for regularization, and  $\delta_{nm}$  is the Kronecker symbol.

Kernel functions are used to quantify the similarity or the amount of covariance between two input feature vectors; several standard families of kernel functions and their combinations are available in the GP and machine learning

literature [27, 28, 38]. Here, we employ two kernel function types: the Radial Basis Function (RBF) kernel and the linear kernel. The RBF kernel is defined as

$$k_{\vec{\theta}}(\vec{X}, \vec{Y}) = \gamma \exp \left( -\frac{\|\vec{X} - \vec{Y}\|^2}{2\sigma^2} \right), \quad (4)$$

where  $\vec{\theta} = (\gamma, \sigma)$ , with  $\gamma$  denoting the amplitude and  $\sigma$  the length scale of the kernel covariance function.

The linear kernel is formulated as

$$k_{\vec{\theta}}(\vec{X}, \vec{Y}) = \theta_1(\vec{X} \cdot \vec{Y}) + \theta_2, \quad (5)$$

where  $\vec{\theta} = (\theta_1, \theta_2)$ , with  $\theta_1$  denoting the scaling term and  $\theta_2$  the offset term.

Next, we write the predictive distribution as

$$p(t_{N+1}|\vec{t}_N) = \int d\lambda_{N+1} p(t_{N+1}|\lambda_{N+1})p(\lambda_{N+1}|\vec{t}_N), \quad (6)$$

where  $p(t_{N+1}|\lambda_{N+1})$  is given by Eq. (1) and

$$p(\lambda_{N+1}|\vec{t}_N) = \int d\vec{\lambda}_N p(\lambda_{N+1}|\vec{\lambda}_N)p(\vec{\lambda}_N|\vec{t}_N). \quad (7)$$

The first probability under the integral in the right-hand side of Eq. (7) is a conditional Gaussian distribution obtained from Eq. (2) in a standard manner [27, 28, 38]:

$$p(\lambda_{N+1}|\vec{\lambda}_N) = \mathcal{N}(\lambda_{N+1}|\vec{k}^T C_N^{-1} \vec{\lambda}_N, c - \vec{k}^T C_N^{-1} \vec{k}), \quad (8)$$

where  $C_N$  is the  $N \times N$  covariance matrix defined as in Eq. (3) for the  $N$  datapoints in the training set,

$$c = k_{\vec{\theta}}(\vec{X}_{N+1}, \vec{X}_{N+1}) + \epsilon, \quad (9)$$

is the value of the kernel function for the new datapoint (plus a small positive constant for regularization), and

$$\vec{k} = [k_{\vec{\theta}}(\vec{X}_1, \vec{X}_{N+1}) \ \dots \ k_{\vec{\theta}}(\vec{X}_N, \vec{X}_{N+1})]^T \quad (10)$$

is a vector of kernel function values for the new datapoint vs.  $N$  datapoints in the training set.

Next, we focus on computing the second probability under the integral in the right-hand side of Eq. (7),  $p(\vec{\lambda}_N|\vec{t}_N)$ . This probability is not Gaussian and therefore has to be computed using the Laplace approximation, so that the multi-dimensional integral in Eq. (7) can be done exactly. Indeed,

$$p(\vec{\lambda}_N|\vec{t}_N) = \frac{p(\vec{t}_N|\vec{\lambda}_N)p(\vec{\lambda}_N)}{p(\vec{t}_N)} \quad (11)$$

by the Bayes theorem. Here, the joint probability

$$p(\vec{\lambda}_N) = \mathcal{N}(\vec{\lambda}_N|\vec{0}, C_N) \quad (12)$$

is generated by the Gaussian process (cf. Eq. (2)) and

$$p(\vec{t}_N|\vec{\lambda}_N) = \prod_{n=1}^N \frac{e^{t_n \lambda_n} e^{-e^{\lambda_n}}}{t_n!} \quad (13)$$

is the product of Poisson probabilities for  $N$  datapoints in the training set (cf. Eq. (1)), with  $\lambda_n = \lambda(\vec{X}_n)$ .

We observe that

$$\log p(\vec{\lambda}_N|\vec{t}_N) = \Psi(\vec{\lambda}_N) - \frac{N}{2} \log(2\pi) - \frac{1}{2} \log(|C_N|) - \sum_{n=1}^N \log(t_n!) - \log p(\vec{t}_N), \quad (14)$$

where  $|C_N|$  is the determinant of  $C_N$  and  $\Psi(\vec{\lambda}_N)$  is the sum of the two terms that depend on the Poisson log-rates:

$$\Psi(\vec{\lambda}_N) = -\frac{1}{2}\vec{\lambda}_N^T C_N^{-1} \vec{\lambda}_N + \sum_{n=1}^N (\lambda_n t_n - e^{\lambda_n}). \quad (15)$$

To find the mean of the multivariate Gaussian in the Laplace approximation for  $p(\vec{\lambda}_N | \vec{t}_N)$ , we need to solve the system of non-linear equations given by

$$\nabla_{\vec{\lambda}_N} \log p(\vec{\lambda}_N | \vec{t}_N) \Big|_{\vec{\lambda}_N = \vec{\lambda}_N^*} = \nabla_{\vec{\lambda}_N} \Psi(\vec{\lambda}_N) \Big|_{\vec{\lambda}_N = \vec{\lambda}_N^*} = \vec{0}, \quad (16)$$

which yields

$$C_N^{-1} \vec{\lambda}_N^* = \vec{D}(\vec{\lambda}_N^*), \quad (17)$$

with  $\vec{D}(\vec{\lambda}_N) = [D_1(\lambda_1) \ \dots \ D_N(\lambda_N)]^T$  and  $D_i = t_i - e^{\lambda_i}$  for  $i \in 1, \dots, N$ .

To find the solution of Eq. (17),  $\vec{\lambda}_N^* = C_N \vec{D}(\vec{\lambda}_N^*)$ , we use the Newton-Raphson (NR) method [39, 40] with a single iterative update defined as

$$\vec{\lambda}_N^{new} = \vec{\lambda}_N^{old} + H^{-1}(\vec{\lambda}_N^{old}) \nabla_{\vec{\lambda}_N} \Psi(\vec{\lambda}_N) \Big|_{\vec{\lambda}_N^{old}} = \vec{\lambda}_N^{old} + H^{-1}(\vec{\lambda}_N^{old}) [\vec{D}(\vec{\lambda}_N^{old}) - C_N^{-1} \vec{\lambda}_N^{old}]. \quad (18)$$

Here,  $H(\vec{\lambda}_N)$  is an  $N \times N$  Hessian matrix given by

$$H(\vec{\lambda}_N) = -\nabla_{\vec{\lambda}_N} \nabla_{\vec{\lambda}_N} \log p(\vec{\lambda}_N | \vec{t}_N) = -\nabla_{\vec{\lambda}_N} \nabla_{\vec{\lambda}_N} \Psi(\vec{\lambda}_N) = C_N^{-1} + W_N(\vec{\lambda}_N), \quad (19)$$

where  $W_{N,ij} \equiv -\frac{\partial D_i}{\partial \lambda_j} = \delta_{ij} e^{\lambda_j}$ , such that  $W_N(\vec{\lambda}_N) = \text{diag}(e^{\lambda_1}, \dots, e^{\lambda_N})$ . Since  $W_N$  is a positive definite matrix,  $H$  is also positive definite and Newton-Raphson iterations are guaranteed to converge, yielding  $\vec{\lambda}_N^*$ , the solution of Eq. (17). The Laplace approximation then yields

$$p(\vec{\lambda}_N | \vec{t}_N) \simeq \mathcal{N}(\vec{\lambda}_N | \vec{\lambda}_N^*, H^{-1}(\vec{\lambda}_N^*)). \quad (20)$$

The multi-dimensional integral in Eq. (7) can now be evaluated, resulting in

$$p(\lambda_{N+1} | \vec{t}_N) = \mathcal{N}(\lambda_{N+1} | \mu, \sigma^2), \quad (21)$$

where

$$\begin{aligned} \mu &= \vec{k}^T C_N^{-1} \vec{\lambda}_N^* = \vec{k}^T \vec{D}(\vec{\lambda}_N^*), \\ \sigma^2 &= c - \vec{k}^T C_N^{-1} \vec{k} + \vec{k}^T C_N^{-1} H^{-1} C_N^{-1} \vec{k} = c - \vec{k}^T (C_N + W_N^{-1})^{-1} \vec{k}. \end{aligned} \quad (22)$$

The probability distribution of  $\alpha_{N+1} = e^{\lambda_{N+1}}$  is log-normal:

$$p(\alpha_{N+1} | \vec{t}_N) = \text{LogNormal}(\alpha_{N+1} | \mu, \sigma^2). \quad (23)$$

Finally, the predictive distribution in Eq. (6) becomes

$$p(t_{N+1} | \vec{t}_N) = \int_{-\infty}^{\infty} d\lambda_{N+1} \frac{e^{t_{N+1} \lambda_{N+1}} e^{-e^{\lambda_{N+1}}}}{t_{N+1}!} \mathcal{N}(\lambda_{N+1} | \mu, \sigma^2) \quad (24)$$

or, equivalently,

$$p(t_{N+1} | \vec{t}_N) = \int_0^{\infty} d\alpha \frac{\alpha^{t_{N+1}} e^{-\alpha}}{t_{N+1}!} \frac{1}{\alpha \sqrt{2\pi\sigma^2}} \exp\left(-\frac{(\ln \alpha - \mu)^2}{2\sigma^2}\right). \quad (25)$$

Thus, the predictive probability distribution is given by the Poisson-LogNormal (PLN) distribution [36, 37] – a convolution between Poisson and log-normal distributions:

$$p(t_{N+1} | \vec{t}_N) = f(t_{N+1}; \mu, \sigma^2) \quad (26)$$

The PLN distribution is a discrete probability distribution normalized over non-negative counts:

$$\sum_{t_{N+1}=0}^{\infty} f(t_{N+1}; \mu, \sigma^2) = 1. \quad (27)$$

Its first two moments are given by  $\mathcal{M}(\vec{X}) \equiv \text{E}[t_{N+1}] = e^{\mu + \frac{\sigma^2}{2}}$  and  $V(\vec{X}) \equiv \text{Var}[t_{N+1}] = e^{\mu + \frac{\sigma^2}{2}} + (e^{\sigma^2} - 1)e^{2\mu + \sigma^2}$ , respectively. Note that  $\mu = \mu(\vec{X})$  and  $\sigma = \sigma(\vec{X})$  depend on the input feature vector  $\vec{X}$  for which the prediction is made.

## B Predictive distribution with prior Poisson rates

In many science and engineering settings, one is faced with a situation where a localized signal needs to be separated from the background noise. In the GP framework, signals can be modeled by introducing a non-zero mean function into the joint probability of observations, Eq. (2) [27, 35]. This mean function serves as a functional prior which biases the functions generated by the Gaussian process before any observations are made. Here, we use the Gaussian process to generate Poisson log-rates, which undergo subsequent non-linear transformations. The nonlinearities make introducing functional priors considerably less trivial. Thus, instead of modifying the underlying Gaussian process, we add the prior function directly to the Poisson rates.

Specifically, we posit that the signal can be represented by a pre-specified non-negative function  $g_{\vec{B}}(\vec{X})$ , where  $\vec{B}$  is a vector of function parameters. For example, a common choice for  $g_{\vec{B}}(\vec{X})$  when  $\vec{X}$  is one-dimensional (i.e.,  $\vec{X} \rightarrow X$ ) is a Gaussian function characterized by the mean  $q$ , the standard deviation  $u$ , and the amplitude  $S$ :

$$g_{\vec{B}}(X) = S \exp \left\{ -\frac{(X - q)^2}{2u^2} \right\}. \quad (28)$$

Here, the vector of function parameters is given by  $\vec{B} = \{S, q, u\}$ .

The total Poisson rate for the input feature  $\vec{X}_{N+1}$  has contributions from both the signal and the background:

$$\alpha_{N+1}^{\text{tot}} = \alpha_{N+1} + g_{\vec{B}}(\vec{X}_{N+1}), \quad (29)$$

or, equivalently,

$$\lambda_{N+1}^{\text{tot}} = \log\{e^{\lambda_{N+1}} + g_{\vec{B}}(\vec{X}_{N+1})\}, \quad (30)$$

showing that the total Poisson log-rate is a function of both the unbiased log-rate and the explicitly defined signal contribution.

The probability distribution of  $\alpha_{N+1}$  is now given by the three-parameter log-normal distribution [41]:

$$\begin{aligned} p(\alpha_{N+1}^{\text{tot}} | \vec{t}_N) &= \text{LogNormal}(\alpha_{N+1}^{\text{tot}} | \mu, \sigma^2, g_{\vec{B}}(\vec{X}_{N+1})) \\ &= \frac{1}{(\alpha_{N+1}^{\text{tot}} - g_{N+1})\sqrt{2\pi\sigma^2}} \exp \left\{ -\frac{(\ln(\alpha_{N+1}^{\text{tot}} - g_{N+1}) - \mu)^2}{2\sigma^2} \right\}, \end{aligned} \quad (31)$$

where  $\mu$  and  $\sigma^2$  are given by Eq. (22) and we have defined  $g_{N+1} = g_{\vec{B}}(\vec{X}_{N+1})$  for brevity. Correspondingly, the predictive distribution is given by

$$p(t_{N+1} | \vec{t}_N) = \int_{g_{N+1}}^{\infty} d\alpha \frac{\alpha^{t_{N+1}} e^{-\alpha}}{t_{N+1}!} \frac{1}{(\alpha - g_{N+1})\sqrt{2\pi\sigma^2}} \exp \left( -\frac{(\ln(\alpha - g_{N+1}) - \mu)^2}{2\sigma^2} \right). \quad (32)$$

This equation is a generalization of Eq. (25) to the case of non-zero prior Poisson rates.

## C Hyperparameter optimization

**Kernel hyperparameters.** Next, we develop a procedure for finding the optimal values of kernel hyperparameters  $\vec{\theta}^*$ . Following a standard approach widely used in Gaussian processes [28], we obtain  $\vec{\theta}^*$  by maximizing the marginal likelihood of the counts observed in the training dataset (cf. Eq. (11)):

$$p(\vec{t}_N | \vec{\theta}) = \int d\vec{\lambda}_N p(\vec{t}_N | \vec{\lambda}_N) p(\vec{\lambda}_N | \vec{\theta}), \quad (33)$$

where the dependence on kernel hyperparameters is made explicit for clarity. Since the multi-dimensional integral on the right-hand side of Eq. (33) cannot be evaluated exactly, we resort once again to the Laplace approximation:

$$\log p(\vec{t}_N | \vec{\theta}) \approx \log p(\vec{\lambda}_N^* | \vec{\theta}) + \log p(\vec{t}_N | \vec{\lambda}_N^*) - \frac{1}{2} \log(|H(\vec{\lambda}_N^*, \vec{\theta})|) + \frac{N}{2} \log(2\pi), \quad (34)$$

where, as before, the numerical values of  $\vec{\lambda}_N^*$  are found by solving Eq. (16) (note that  $\Psi(\vec{\lambda}_N)$  contains all the  $\vec{\lambda}_N$ -dependent terms in  $\log[p(\vec{\lambda}_N|\vec{\theta})p(\vec{t}_N|\vec{\lambda}_N)]$ ).

The optimized hyperparameters  $\vec{\theta}^*$  are found as

$$\operatorname{argmax}_{\vec{\theta}} \left\{ \Psi(\vec{\lambda}_N^*(\vec{\theta})) - \frac{1}{2} \log |\mathbb{1}_N + C_N(\vec{\theta})W_N(\vec{\lambda}_N^*(\vec{\theta}))| \right\}, \quad (35)$$

where  $\mathbb{1}_N$  is an  $N \times N$  unit matrix.

The maximization in Eq. (35) is carried out as follows: for a fixed value of  $\vec{\theta}$ , the corresponding values of  $\vec{\lambda}_N^*(\vec{\theta})$  are found via NR iterations of Eq. (16) (cf. Eq. (18)). These values are then substituted into Eq. (35), providing a point estimate of the argmax argument. The maximization with respect to  $\vec{\theta}$  is done using the L-BFGS-B algorithm (Limited-memory Broyden-Fletcher-Goldfarb-Shanno algorithm with Box constraints) [42–45] implemented in the SciPy library [46]. Note that the box constraints in the SciPy L-BFGS-B implementation allow us to restrict any hyperparameter to a prespecified range, ensuring that the covariance matrix remains positive semi-definite. In particular, we enforce  $\theta_1 > 0$  and  $\theta_2 > 0$  hyperparameter ranges in the linear kernel (Eq. (5)). First derivatives of the argmax argument with respect to  $\vec{\theta}$  are evaluated numerically using finite differences. The L-BFGS-B maximization yields the optimal vector of hyperparameters  $\vec{\theta}^*$  which is used in subsequent predictions.

**Signal parameters.** When the prior Poisson rates are included, we need to consider

$$p(\vec{t}_N|\vec{\theta}, \vec{B}) = \int d\vec{\lambda}_N p(\vec{t}_N|\vec{\lambda}_N^{\text{tot}})p(\vec{\lambda}_N|\vec{\theta}), \quad (36)$$

where, similar to Eq. (30),  $\lambda_n^{\text{tot}} = \log(e^{\lambda_n} + g_n)$ ; we have defined  $g_n = g_{\vec{B}}(\vec{X}_n)$  for brevity. Note that we do not modify the zero mean in the joint probability  $p(\vec{\lambda}_N|\vec{\theta})$  (Eq. (2)); only the conditional probability of the observed counts depends on  $\vec{B}$  explicitly:  $p(\vec{t}_N|\vec{\lambda}_N) \rightarrow p(\vec{t}_N|\vec{\lambda}_N^{\text{tot}}) = p(\vec{t}_N|\vec{\lambda}_N, \vec{B})$ . Although in principle the marginal log-likelihood,  $\log p(\vec{t}_N|\vec{\theta}, \vec{B})$ , needs to be maximized with respect to both the hyperparameters  $\vec{\theta}$  and the prior function parameters  $\vec{B}$ , we carry out the maximization in two separate stages in order to ensure robust signal-background separation.

We focus on the prior signal functions localized in the feature space, such as the one-dimensional Gaussian in Eq. (28). We divide the training data into the ‘background only’ and ‘signal+background’ datasets (this requires the region of the feature space in which the signal is located to be approximately known in advance) and fit the parameters in two steps. First, we find  $\vec{\theta}^*$  using the background-only dataset, under the assumption that  $g_{\vec{B}} = 0$  (Eq. (35)). Second, we find  $\vec{B}^*$  using the signal+background dataset and maximizing  $\log p(\vec{t}_N|\vec{\theta}^*, \vec{B})$  with respect to  $\vec{B}$ , while keeping  $\vec{\theta} = \vec{\theta}^*$ . Note that the kernel hyperparameters are not modified in the second stage and therefore capture the properties of the background, while the prior function parameters are used to describe the contribution of the signal.

Under the Laplace approximation, Eq. (36) yields:

$$\log p(\vec{t}_N|\vec{\theta}^*, \vec{B}) \approx \log p(\vec{\lambda}_N^*|\vec{\theta}^*) + \log p(\vec{t}_N|\vec{\lambda}_N^{\text{tot},*}) - \frac{1}{2} \log(|H(\vec{\lambda}_N^*, \vec{\theta}^*, \vec{B})|) + \frac{N}{2} \log(2\pi), \quad (37)$$

where  $N$  now denotes the number of datapoints in the signal+background dataset. We find  $\vec{\lambda}_N^*$  by solving

$$\nabla_{\vec{\lambda}_N} \Psi(\vec{\lambda}_N, \vec{B}) \Big|_{\vec{\lambda}_N = \vec{\lambda}_N^*} = \vec{0}, \quad (38)$$

where

$$\Psi(\vec{\lambda}_N, \vec{B}) = -\frac{1}{2} \vec{\lambda}_N^T C_N^{-1} \vec{\lambda}_N + \sum_{n=1}^N (\lambda_n^{\text{tot}} t_n - e^{\lambda_n^{\text{tot}}}). \quad (39)$$

Eq. (38) yields

$$C_N^{-1} \vec{\lambda}_N^* = \vec{D}(\vec{\lambda}_N^*, \vec{B}), \quad (40)$$

where  $\vec{D}_i = t_i/(1 + g_i e^{-\lambda_i}) - e^{\lambda_i}$  for  $i \in 1, \dots, N$ . As before, Eq. (40) can be solved by the NR method, which requires the Hessian matrix (also used in Eq. (37)):

$$H(\vec{\lambda}_N, \vec{\theta}^*, \vec{B}) = -\nabla_{\vec{\lambda}_N} \nabla_{\vec{\lambda}_N} \Psi(\vec{\lambda}_N, \vec{B}) = C_N^{-1} + \widetilde{W}_N(\vec{\lambda}_N, \vec{B}), \quad (41)$$

where

$$\widetilde{W}_{N,ij} = \delta_{ij} \left[ e^{\lambda_j} - \frac{t_i g_i e^{-\lambda_i}}{(1 + g_i e^{-\lambda_i})^2} \right]. \quad (42)$$

Finally, the optimized signal parameters  $\vec{B}^*$  are found via

$$\operatorname{argmax}_{\vec{B}} \left\{ \sum_{n=1}^N [t_n \log(e^{\lambda_n^*} + g_n) - e^{\lambda_n^*} - g_n] - \frac{1}{2} \log |C_N^{-1} + \widetilde{W}_N(\vec{\lambda}_N^*, \vec{B})| \right\}. \quad (43)$$

As before, the maximization can be done using L-BFGS-B, yielding the optimal vector of signal function parameters  $\vec{B}^*$ . Note that, in general,  $\vec{\lambda}_N^* = \vec{\lambda}_N^*(\vec{B})$  and thus  $\vec{\lambda}_N^*$  needs to be recomputed as  $\vec{B}$  is updated, even if  $\theta = \theta^*$  in Eq. (43).

**The weak-signal approximation.** In many situations, we expect the signal to be relatively weak compared to the background. If the observed Poisson counts are dominated by the background contribution, we have  $g_n e^{-\lambda_n^*} = g_n / \alpha_n^* \ll 1, \forall n$ . Since  $\vec{D} \rightarrow \vec{D}$  and  $\widetilde{W}_N \rightarrow W_N$  in this limit, the optimization procedure becomes considerably simplified. Indeed,  $\vec{\lambda}_N^*(\theta^*)$  can now be found *once* using Eq. (17) since it is independent of  $\vec{B}$ . Consequently, Eq. (43) simplifies to

$$\operatorname{argmax}_{\vec{B}} \left\{ \sum_{n=1}^N [t_n \log(e^{\lambda_n^*} + g_n) - g_n] \right\}. \quad (44)$$

Setting the  $\partial/\partial B_i$  derivatives of the argmax argument in Eq. (44) to 0, we obtain the following self-consistency condition:

$$\sum_{n=1}^N \frac{t_n}{e^{\lambda_n^*} + g_n} \frac{\partial g_n}{\partial B_i} = \sum_{n=1}^N \frac{\partial g_n}{\partial B_i}, \quad (45)$$

where  $\vec{B} = \vec{B}^*$  everywhere. Note that Eq. (45) is consistent with  $t_n \simeq \alpha_n^* + g_n^* (\forall n)$ , such that each observation is modeled as a sum of the background and signal contributions with optimized parameters.

### III Results

#### A Synthetic datasets

We start by applying the PoLoN methodology described in Section II A to several one-dimensional (1D) synthetic datasets. For each dataset, we postulate  $\alpha(x)$ , a function which describes the dependence of the Poisson rate on the 1D input feature  $x$ . We choose a set of  $M$  equidistant values of  $x$  within a pre-specified range,  $\{x_i\}_{i=1}^M$ , and sample  $N_p$  datapoints for each  $x_i$  such that the total number of observations is  $N = MN_p$ . We use these data to model the Poisson rates (Eq. (23)) and construct the predictive distribution (Eq. (25)). The kernel hyperparameters are found by optimizing the marginal log-likelihood (Eq. (34)) with the L-BFGS-B algorithm, as described above.

Our first 1D example is a system in which Poisson rates follow a linear trend with superimposed oscillations (Fig. 1a,b). The blue curve in Fig. 1a shows the mean of the Poisson-LogNormal predictive distribution (Eq. (25)), which is equal to the mean of the LogNormal distribution of the predicted Poisson rates (Eq. (23)) and therefore can be compared directly with the exact Poisson rates  $\alpha(x) = ax + A \sin(2\pi\nu x)$  (red curve in Fig. 1a;  $a = 1$ ,  $A = 5$ ,  $\nu = 50.075$ ). Our prediction is based on  $M = 50$  equidistant values of  $x$  in the  $[1, 50]$  range; for each value  $x_i$  in the dataset ( $i = 1 \dots 50$ ),  $N_p = 8$  datapoints were randomly generated from a Poisson distribution with  $\alpha(x_i)$ , resulting in a training set with  $N = 400$  points in total. We used the RBF kernel (Eq. (4)) with hyperparameters  $\sigma^* = 6.999$  and  $\gamma^* = 11.880$  that maximize the posterior log-likelihood (Fig. 2).

We find an excellent overall agreement between predicted and exact Poisson rates, with the root-mean-square error (RMSE)  $\delta = 0.907$  over  $W = 500$  equally spaced points in the  $[1, 50]$  training data range (Fig. 1a), where  $\delta = W^{-1/2} \sqrt{\sum_{j=1}^W [\alpha(x_j) - \mathcal{M}(x_j)]^2}$ , where  $\mathcal{M}(x_j)$  is the mean of the predictive distribution at position  $x_j$  and  $\alpha(x_j)$  is the exact Poisson rate. Thus, our approach can be used to extract unknown Poisson rates from noisy data

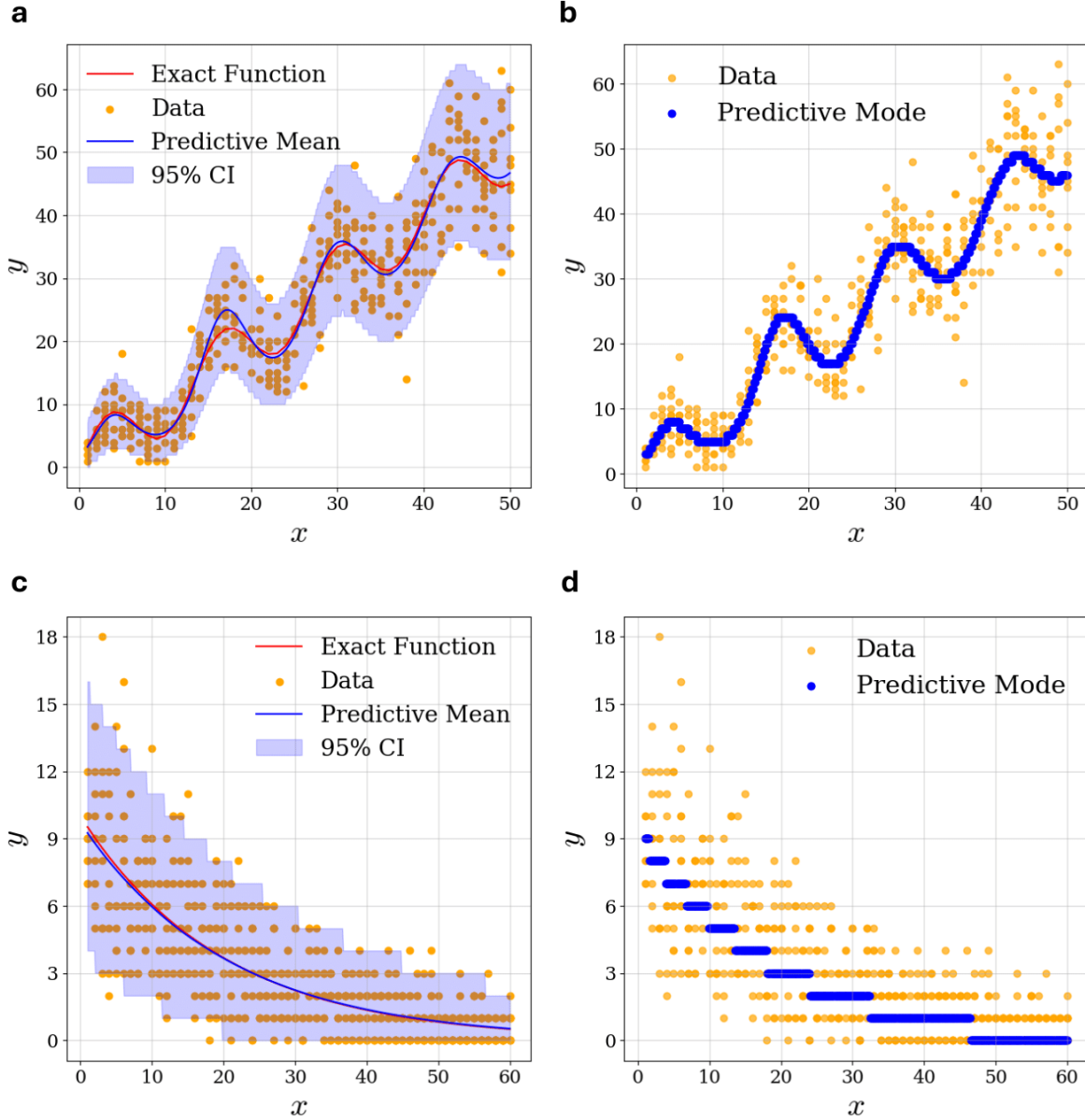


**FIG. 1: PoLoN predictions for 1D integer-count data.** Panel (a) shows exact Poisson rates  $\alpha(x)$  that follow a linear trend with superimposed oscillations (red curve). Training set datapoints are shown as yellow dots. Blue curve: mean of the predictive PLN distribution, light blue shaded area: 95% confidence interval (CI). Panel (b) shows the training set datapoints (yellow dots) and the modes of the predictive PLN distributions for  $W = 500$  values of  $x$  equally spaced in the training dataset range. The modes represents maximum posterior probability (MAP) predictions. Panels (c-d) – same as (a-b) but for the exponentially decaying  $\alpha(x)$ .

and interpolate between the observed values of  $x_i$ . Since our predictions are Bayesian, we can also estimate their uncertainty, quantified as the 95% confidence interval (CI) in Fig. 1a,c and elsewhere. We also plot the mode of the Poisson-LogNormal predictive distribution (Eq. (25)), which corresponds to the most probable integer count at each of the  $W = 500$  points for which our predictions were made (Fig. 1b).

Our next 1D example is a Poisson rate function which combines a quadratic curve with sinusoidal modulation:  $\alpha(x) = ax^2 + bx + c + A \sin(2\pi\nu x)$ , with  $a = 0.1$ ,  $b = 1$ ,  $c = 2$ ,  $A = 5$ , and  $\nu = 0.15$  (Fig. S1a,b). Similarly to

the previous example, we used this function to generate  $N_p = 8$  Poisson counts at  $M = 30$  values of  $x_i$  that are equally spaced in the  $[1, 30]$  range. Here, we employed the RBF kernel (Eq. (4)) with  $\sigma^* = 3.635$  and  $\gamma^* = 8.008$  hyperparameters corresponding to the maximum of the posterior log-likelihood (Fig. S2a). The PoLoN procedure captures both the quadratic and sinusoidal trends in the data (Fig. S1a,b), with the RMSE error  $\delta = 6.635$  for  $W = 500$  equally spaced points within the  $[1, 30]$  range.

Next, we checked whether the PoLoN procedure can capture a purely periodic signal,  $\alpha(x) = A \sin(2\pi\nu x) + k$ , with  $A = 50$ ,  $\omega = 0.5$ , and  $k = 60$  (Fig. S1c,d). The training dataset contains 400 datapoints:  $N_p = 8$  and  $M = 50$ , with  $x_i$  equally spaced in the  $[1, 50]$  range. Again, the RBF kernel (Eq. (4)) was used, with optimized hyperparameters  $\sigma^* = 2.739$  and  $\gamma^* = 8.173$  (Fig. S2b). The PoLoN procedure is capable of reproducing the purely sinusoidal trend (Fig. S1c,d), with the RMSE error  $\delta = 2.191$  for 500 equally spaced points within the  $[1, 50]$  range.

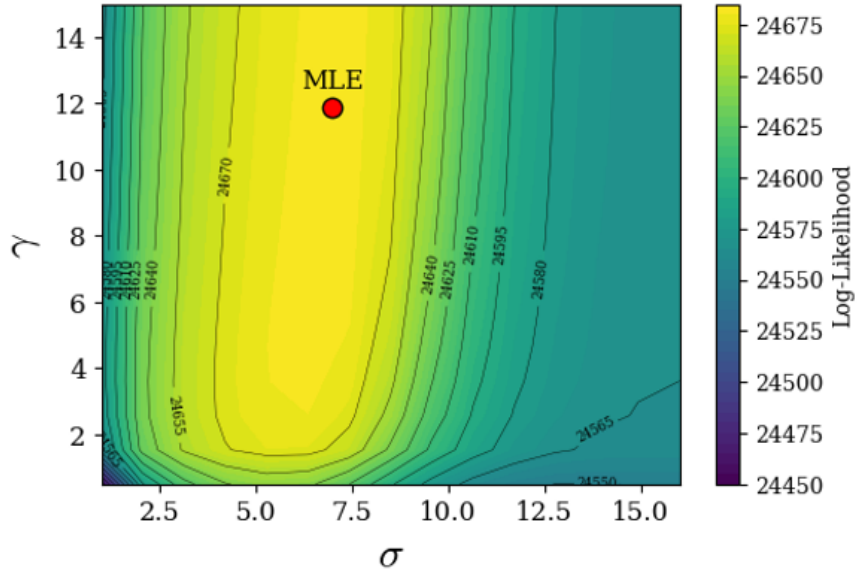


FIG. 2: **Kernel hyperparameter optimization.** Contour-overlaid heatmap of the posterior log-likelihood (Eq. (34)) for the training dataset generated by  $\alpha(x)$  which consists of a linear trend with superimposed oscillations (Fig. 1a). The optimal (Maximum Likelihood Estimation, or MLE) hyperparameters  $\sigma^* = 6.999$  and  $\gamma^* = 11.880$ , found using the L-BFGS-B algorithm, are marked with a red dot.

Our final 1D example focuses on a training dataset generated using the exponentially decaying Poisson rate function which mimics commonly found background distributions:  $\alpha(x) = Ae^{-\kappa x}$ , with  $A = 10$  and  $\kappa = 0.05$  (Fig. 1c,d). We chose  $N_p = 10$  and  $M = 60$ , with  $x_i$  equally spaced in the  $[1, 60]$  range. In contrast to the three previous examples, we used a linear kernel (Eq. (5)) with optimized parameters  $\theta_1^* = 0.0025$  and  $\theta_2^* = 8.500$  (Fig. S2c). Linear kernels are well-suited to a linear trend in log space produced by the exponentially decaying  $\alpha(x)$ . As can be seen in Fig. 1c, there is an excellent agreement between the predicted and exact Poisson rate curves, with  $\delta = 0.463$  for  $W = 500$  equally spaced points within the original  $[1, 60]$  range.

Next, we applied our methodology to a more challenging dataset with 2D input features arranged on an  $(x, y)$  grid. The dataset was generated using a Poisson rate function  $\alpha(x, y) = ax + b \sin(cy) + d$  with parameters  $a = 0.8$ ,  $b = 3.0$ ,  $c = 0.5$ , and  $d = 1.0$  (Fig. 3a). We used a  $15 \times 15$  grid of equally spaced points with  $x, y \in [1, 29]$  (i.e.,  $x_i, y_j = \{1, 3, \dots, 29\}$ ;  $i, j = 1 \dots 15$ ). For each  $(x, y)$  pair, the corresponding rate parameter  $\alpha(x, y)$  was computed and  $N_p = 4$  Poisson-distributed counts were generated at each of the  $M = 15^2$  grid points. Thus, the training dataset consists of  $N = 900$  points (Fig. 3a). For testing, we constructed a separate  $15 \times 15$  grid of equally spaced points with  $x, y \in [2, 30]$  (i.e.,  $x_i, y_j = \{2, 4, \dots, 30\}$ ;  $i, j = 1 \dots 15$ ), interspersed with the training datapoints. We employed the RBF kernel with hyperparameters  $\sigma^* = 6.898$  and  $\gamma^* = 6.804$  corresponding to the maximum of the posterior log-likelihood (Fig. S2d). Figure 3b shows the mean of the predictive distribution versus exact Poisson rates on a set of 225  $(x, y)$  pairs that were not used in training the model. Our model exhibits high accuracy in predicting the 2D Poisson rates ( $R^2 = 0.982$ ).

Finally, we have constructed a collection of synthetic datasets inspired by the discovery of the Higgs boson [1, 2, 47] and the ongoing search for new physics at the Large Hadron Collider (LHC) at CERN [48]. Our objective is to emulate the Higgs boson signal superimposed on a smoothly varying background. We model the background using an exponentially decaying function and represent the Higgs boson signal as a single Gaussian peak [35]. Accordingly,

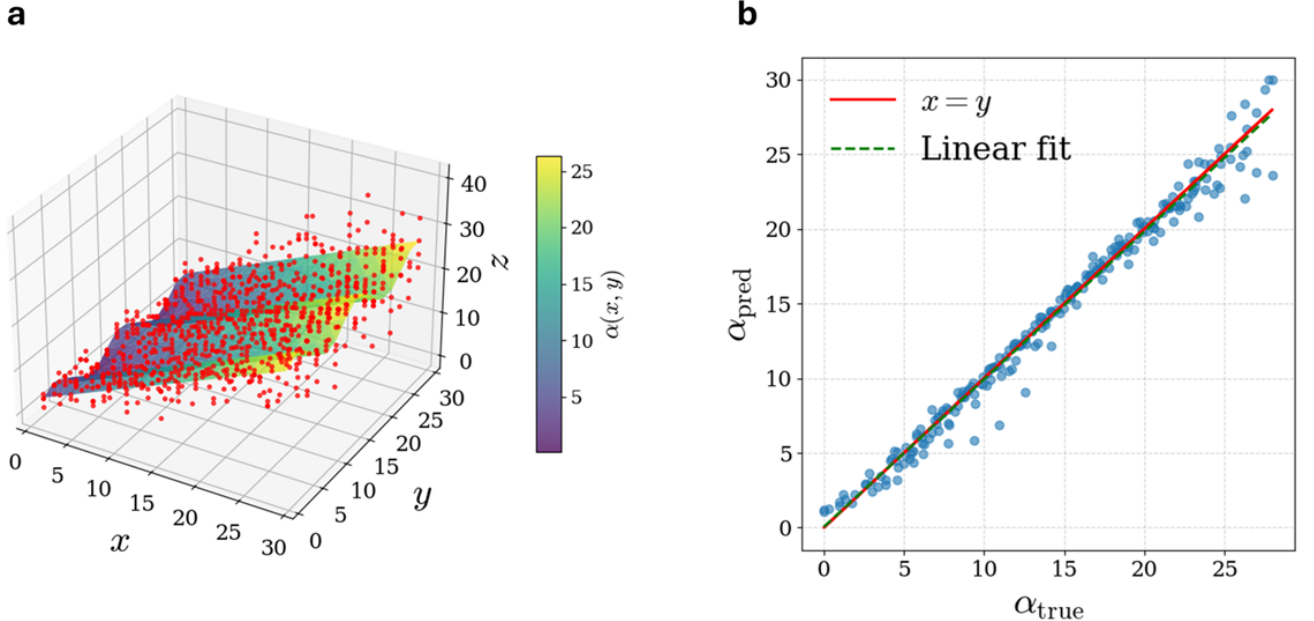


FIG. 3: **PoLoN predictions for 2D integer-count data.** Panel (a) shows the two-dimensional Poisson rate function  $\alpha(x, y)$  with a linear trend in the  $x$ -direction and oscillations in the  $y$ -direction, for  $x, y \in [1, 30]$ . The training datapoints are shown in red. Panel (b) shows a comparison between predicted and actual Poisson rates for 225  $(x, y)$  pairs in the test set. The solid red line is the “ $x = y$ ” line; the dashed green line is the least-squares fit. The coefficient of determination is  $R^2 = 0.982$ .

we define the Poisson rate function as

$$\alpha(x) = Ae^{-\kappa x} + S \exp \left\{ -\frac{(x - q)^2}{2u^2} \right\}, \quad (46)$$

where  $\log A = 11.7$ ,  $\kappa = 30.6$ ,  $q = 0.135$ , and  $u = 0.004$ . These parameters are chosen to mimic the  $H \rightarrow \gamma\gamma$  invariant mass plot (the  $m_{\gamma\gamma}$  mass distribution) reported for the Higgs boson [2], with  $x$  representing the invariant mass of a photon pair,  $m_{\gamma\gamma}$ , measured in TeV.

In the following, we vary the signal strength parameter  $S$  to assess the accuracy of our methodology in detecting the Gaussian peak; see representative Poisson rate curves in Fig. S3. To create a training dataset, we select  $M = 40$  equally spaced data points in the range  $x \in [0.1, 0.16]$  and use Eq. (46) to generate  $N_p$  Poisson counts at each value of  $x$ . We use the approach described in Section II A (PoLoN) and follow the procedure used in the preceding synthetic examples: (i) generate training set counts using Eq. (46), (ii) determine the hyperparameters that maximize the posterior log-likelihood, and (iii) use optimal hyperparameter values for prediction. In this approach, signal is not explicitly separated from the background. In addition, we employ the method described in Section II B (PoLoN-SB) for the same datasets. In this approach, we explicitly predict the signal parameters (signal strength  $S$ , mean  $q$ , and standard deviation  $u$ ) under the assumption that the signal is represented by a single Gaussian peak. These predictions can be compared with the exact values used in the Poisson rate function (Eq. (46)).

We first assess the ability of both methods to capture the signal by calculating the normalized root-mean-square error (RMSE) in the  $\pm 2u$  window around  $q$ :

$$\epsilon = \frac{\text{RMSE}_{2u}}{S} \times 100, \quad (47)$$

where the known signal strength  $S$  is used for normalization, such that the RMSE is reported as the percentage of  $S$ . We use the  $\pm 2u$  window to focus on the accuracy of signal prediction; we already know that exponentially decaying backgrounds can be accurately modeled by our approach (Fig. 1c,d). As before, the RMSE was computed using the squared differences between the mean of the predictive distribution  $\mathcal{M}(x_i)$  and the exact Poisson rates  $\alpha(x_i)$  (Eq. (46)), where  $x_i$  refer to the 11 values of  $x$  from the training dataset that fall in the  $\pm 2u$  window: [0.127, 0.143].

Figure 4 shows the relative error  $\epsilon$  (Eq. (47)) between the PoLoN and PoLoN-SB methods as a function of the total number of datapoints in the training set. We find that, as expected, the quality of the fit improves with  $N_p$  for both

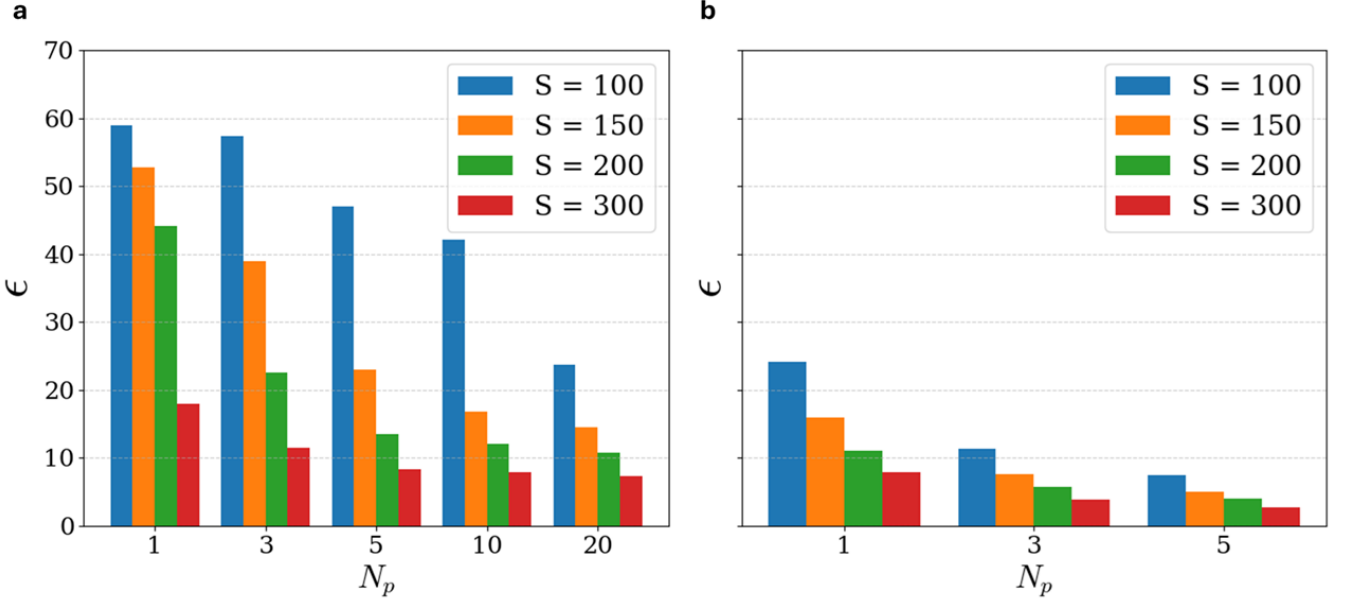


FIG. 4: Normalized RMSE as a function of  $N_p$ , the number of datapoints per input feature  $x$  in the training dataset. Panel (a) shows  $\epsilon$  for PoLoN predictions (Section II A). Panel (b) shows  $\epsilon$  for PoLoN-SB predictions (Section II B). For each combination of  $N_p$  and  $S$ , the normalized RMSE  $\epsilon$  in Eq. (47) was averaged over 10 independently generated training datasets.

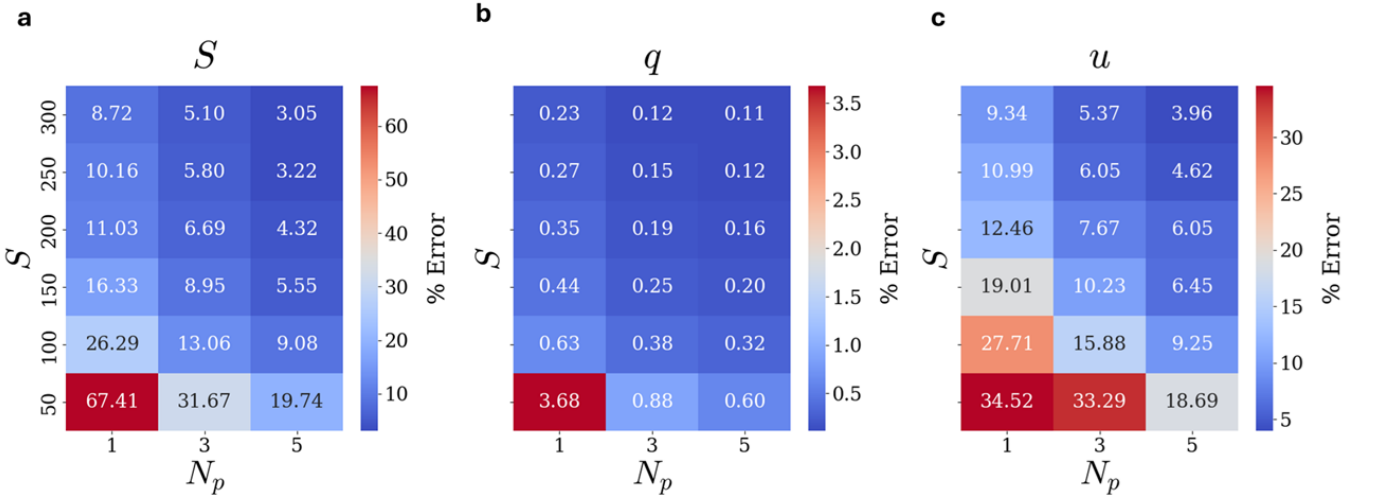


FIG. 5: Relative percentage error in signal parameter predictions. Panel (a) shows the error in the predicted signal strength  $S$ , panel (b) shows the error in the predicted mean of the signal  $q$ , and panel (c) shows the error in the predicted standard deviation of the signal  $u$ . We used PoLoN-SB (Section II B) to predict the signal parameters. For each combination of  $N_p$  and  $S$ , the relative percentage error (computed as  $\frac{|predicted - true|}{true} \times 100\%$ ) was averaged over 10 independently generated training datasets.

methods. Additionally, for a fixed  $N_p$ , increasing the signal strength enhances the fitting accuracy. Importantly, for the same values of  $N_p$  and  $S$  PoLoN-SB demonstrates superior performance compared to PoLoN.

Next, we evaluate how precisely the Gaussian signal parameters are recovered using PoLoN-SB (Section II B). Figure 5 displays percentage errors in the predicted amplitude  $S$ , mean  $q$ , and standard deviation  $u$  of the Gaussian peak as a function of the signal strength  $S$  and the number of datapoints per input feature  $N_p$  in the training set. Thus, we are able to track the accuracy of parameter recovery as  $S$  and  $N_p$  are varied, complementing the analysis

presented in Figure 4. As expected, prediction accuracy improves with increasing both signal strength  $S$  and the number of datapoints per input feature  $N_p$ . The relative errors are comparable in magnitude for  $S$  and  $u$  (Fig. 5a,c) and smaller for  $q$  (Fig. 5b). Overall, we conclude that PoLoN-SB can be used to reliably predict signal parameters for relatively weak signal strengths and moderate training set sizes.

## B Real-world datasets

**Bike rental counts.** We have trained the PoLoN model (Section II A) on a standard machine learning dataset containing both hourly and daily counts of rental bikes from 2011 to 2012 for the Capital Bikeshare program in Washington, D.C. (<https://www.kaggle.com/datasets/lakshmi25npathi/bike-sharing-dataset>) [49]. We focus on the hourly counts and use the hour of the day  $t_h$  and the day of the week  $t_d$  as two entries in the input feature vector (the dataset provides several features such as the hour of the day, the day of the week, whether the day was a working day or a holiday, and the weather conditions (cloudy or sunny)). We combine observations for the odd hours in the first three weeks of bike-sharing data to train the PoLoN model (Fig. 6a), checking the accuracy of our predictions against the even-hour bike rental numbers in the same three weeks (Fig. 6b,c). We have used the RBF kernel with optimized hyperparameters  $\sigma^* = 2.201$  and  $\gamma^* = 7.378$ .

We observe an excellent agreement between the odd-hour training data and the model, with  $R^2 = 0.907$  (the  $R^2$  values were computed for training set datapoints vs. the predictive mean  $\mathcal{M}(t_h, t_d)$  at each hour; see Fig. 6a). Furthermore, our model demonstrates a reasonable ability to interpolate, with  $R^2 = 0.841$  on the test set which comprises bike rental observations in the even hours over the same three-week period (Fig. 6b; the  $R^2$  values were computed as for the training set). We conclude that our model can use fairly limited data to capture and generalize complex signals often observed in real-world datasets.

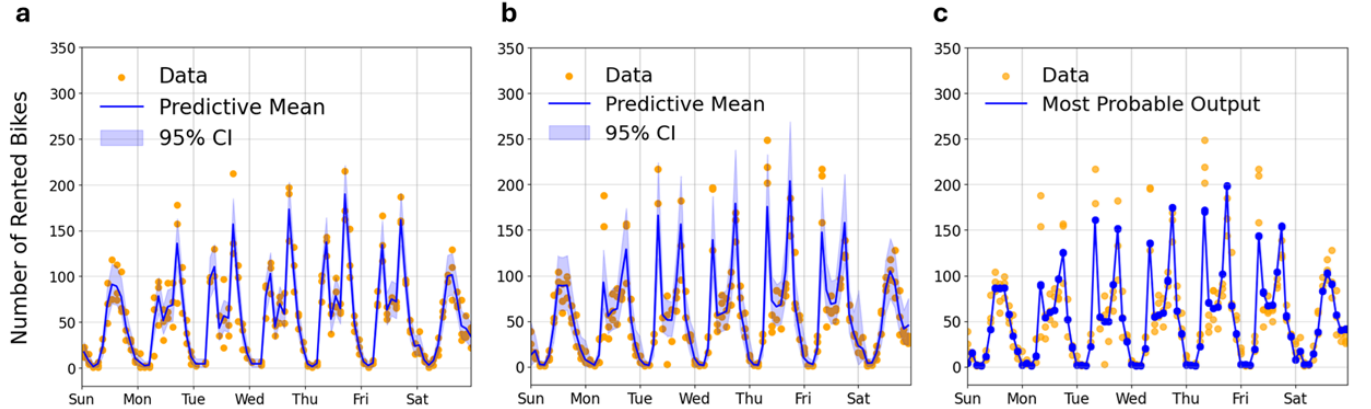


**FIG. 6: PoLoN modeling of the bike rental dataset.** In all three panels, yellow dots represent observations (training set in (a), test set in (b) and (c)) and the horizontal axes show the time of the week, starting from the beginning of Sunday. In panels (a) and (b), the blue line shows the mean of the predictive distribution and the shaded blue region indicates the 95% CI of the prediction. Panel (a) shows the model fit on the training set (three-week bike renting data, odd hours), with optimized hyperparameters  $\sigma^* = 2.201$  and  $\gamma^* = 7.378$ . Panel (b) shows the the mean and the 95% CI of the predictive distribution for the test set (three-week bike renting data, even hours); the hyperparameters are the same as in (a). In panel (c), blue points represent the mode of the predictive distribution for the test set; the connecting blue lines are added to guide the eye.

**Higgs boson discovery.** In this section, we focus on extracting the Higgs boson signal from the Quantum Chromodynamics (QCD) background. The discovery of the Higgs boson at the LHC in July of 2012 [1, 2] provided crucial experimental confirmation for the mechanism of mass acquisition by fundamental particles in the Standard Model of particle physics [47]. We have used the open dataset made available by the ATLAS collaboration at LHC and employed the selection criteria as documented in Ref. [50] to create a di-photon invariant mass distribution,  $m_{\gamma\gamma}$ . The  $m_{\gamma\gamma}$  distribution shows the Higgs boson decay as a localized bump superimposed on the smooth background [50]. The Higgs boson dataset provides an ideal test case for the separation of weak localized signals from smoothly varying background distributions. This task is relevant to many areas of physics and chemistry, with potential applications ranging from exoplanet detection [12, 13] to XPS spectroscopy [5–7].

We employ PoLoN-SB (Section II B) since it shows better performance in capturing the overall shape of the signal+background curve (Fig. 4) and is capable of extracting the parameters of the Gaussian signal (Fig. 5). As in our previous work [35], we assume that the window in which the Higgs signal is located is approximately known. Consequently, we exclude the  $0.12 \leq m_{\gamma\gamma} \leq 0.13$  TeV region and fit the background-only model (dashed green line in Fig. 7a, upper panel). This background-only model yields optimized hyperparameters  $\sigma^* = 0.108$  and  $\gamma^* = 21.253$  for the RBF kernel.

These hyperparameters, which represent the properties of the background, are then used to estimate the parameters of the Gaussian signal, yielding  $S^* = 321.675$ ,  $q^* = 0.12457$ , and  $u^* = 0.001247$ . The mean and the 95% CI of the full signal+background predictive distribution are displayed in the upper panel of Fig. 7a. The lower panel shows the Z-scores with respect to the background-only model in each energy bin, which clearly demonstrate the background-signal separation (Fig. 7a, lower panel). The Z-score reaches a maximum of 4.45 at  $m_{\gamma\gamma} = 0.1248$  TeV, indicating that the signal is highly statistically significant.

The modes (MAP predictions) of the background-only and signal+background predictive distributions are shown in the upper panel of Fig. 7b, with the lower panel showing the difference  $\Delta$  between the two modes. We estimate the total number of excess events due to the Higgs boson decay to be 1657 in the  $[0.12, 0.13]$  TeV ( $[120, 130]$  GeV) signal window; only one of the  $\Delta$  values is negative in this range.

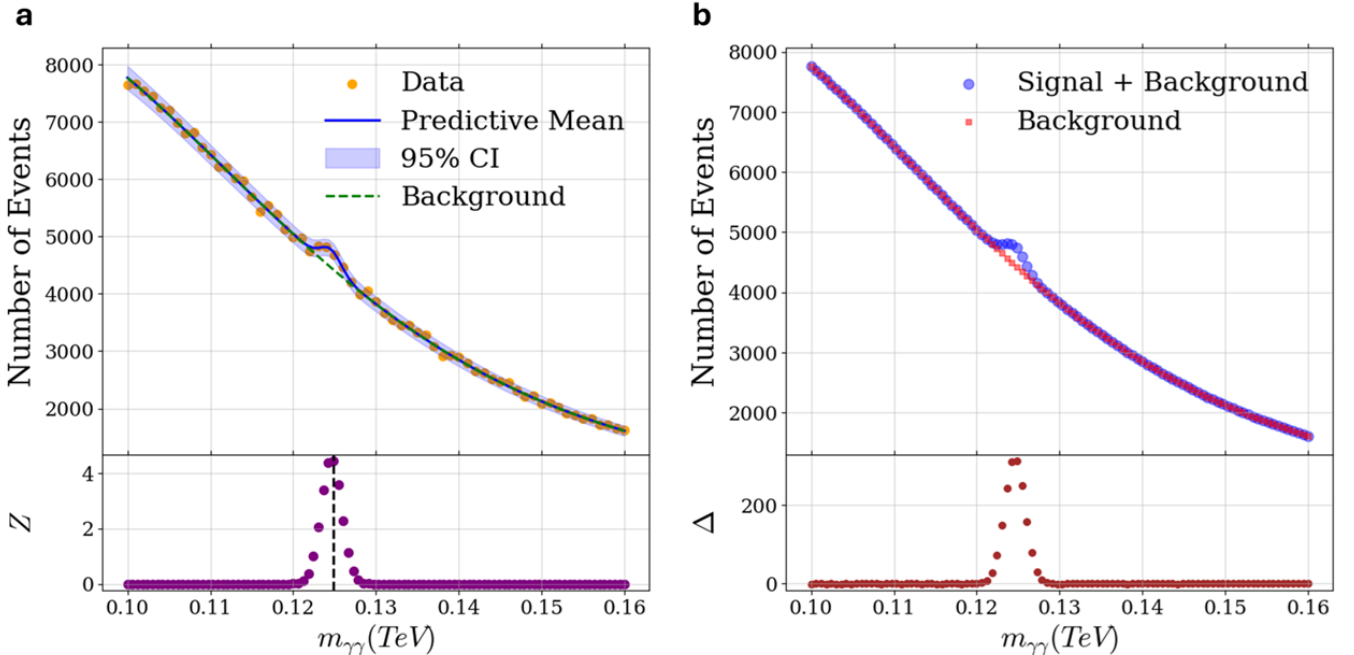


**FIG. 7: Detection of the Higgs boson decay events.** (a) In the upper panel, yellow dots represent the number of events observed in each energy bin. In total, there are 100 equal-width bins in the  $[0.10, 0.16]$  TeV range. The mean of the background-only predictive distribution (fitted on the data outside of the  $[0.12, 0.13]$  TeV signal window) is shown as a dashed green curve. The mean of the signal+background predictive distribution is shown as a solid blue curve, with the 95% CI highlighted in light blue. In the lower panel, we plot the Z-scores with respect to the background-only predictive distribution:  $Z = V_b^{-1/2}(\mathcal{M}_{sb} - \mathcal{M}_b)$ , where  $\mathcal{M}_{sb}$ ,  $\mathcal{M}_b$ ,  $V_b$  are the mean of the signal+background predictive distribution and the mean and the variance of the background-only predictive distribution, respectively. The vertical dashed line indicates the location of the maximum Z-score:  $Z_{max} = 4.45$  at  $m_{\gamma\gamma}^* = 0.1248$  TeV. (b) In the upper panel, blue circles represent the mode  $\tilde{\mathcal{M}}_{sb}$  of the signal+background predictive distribution; red squares denote the mode  $\tilde{\mathcal{M}}_b$  of the background-only predictive distribution. In the lower panel, we plot the difference between the two MAP predictions:  $\Delta = \tilde{\mathcal{M}}_{sb} - \tilde{\mathcal{M}}_b$ .

## IV Discussion and Conclusion

In this work, we have adapted the Gaussian process framework to modeling non-negative count data. In our approach, the Poisson log-rates are represented by the Gaussian process, which ensures non-negativity of the predicted Poisson rates and results in the Poisson-LogNormal (PLN) predictive distribution [36]. Gaussian processes provide a non-parametric Bayesian alternative to basis function fits – instead of explicitly fitting a set of basis function weights, they employ kernel functions which capture correlations between datapoints and depend on only a few hyperparameters [27, 28].

We have demonstrated that our computational approach, which we call the Poisson Log-Normal (PoLoN) process, can be used to make novel predictions and extract the underlying Poisson rate function from limited-size synthetic datasets. The predicted Poisson rate functions can be interpreted as de-noised representations of the observed integer count data. We have also used the PoLoN framework to make predictions of the hourly numbers of bike rentals observed in 2011-2012 for the Capital Bikeshare program in Washington, D.C.

We have focused in particular on the problem of decomposing the observed event counts into the contributions due to a localized signal and a smoothly varying background. As discussed in the Introduction, this problem occurs in many areas of science and often involves low-dimensional datasets in which observations are recorded as a function of 1D or 2D position, time, energy, wavelength, or frequency. To address the problem of signal-background separation, we have developed a version of PoLoN, which we call PoLoN-SB, in which the signal contribution to the Poisson rates is modeled explicitly by a function with a few additional fitting parameters.

The PoLoN-SB approach proceeds in two stages. First, we model the background distribution by excluding the signal window, obtaining kernel hyperparameters for the background-only model. Second, we keep the kernel hyperparameters fixed and fit the signal parameters on the entire dataset, using an explicit functional form to represent the signal. In this way, we achieve robust decomposition of the total set of observations into background and signal components. After checking the performance of PoLoN-SB on an extensive collection of synthetic datasets with varying signal strengths and dataset sizes, we use our approach to separate Higgs boson decay events from the QCD background on a dataset similar to that used to report the Higgs boson discovery at the LHC in 2012 [1]. We find that, in line with previous analyses [1, 2, 35], PoLoN-SB assigns high statistical significance to the Higgs boson signal.

There are several principal directions in which our computational framework can be further developed in the future. First of all, a more general approach would scan for (potentially multiple) signal locations rather than assume that the signal position is both unique and approximately known *a priori*. It would also be of interest to explore replacing the Poisson distribution with the negative binomial distribution, which would allow for modeling datasets with overdispersion [22, 24, 51]. While in this work we relied principally on the RBF kernel, future work could explore automated kernel engineering and selection [52, 53]. For datasets with multi-dimensional feature vectors, automatic relevance determination (ARD) could be used to identify and select the most important features, reducing the effective dimensionality of the data and thus mitigating computational costs [27, 28]. Finally, one could explore the scalability of the PoLoN approach to larger and higher-dimensional datasets using sparse Gaussian processes [54–56].

In conclusion, PoLoN offers a flexible and robust approach to modeling count data across diverse scientific and engineering applications. With continued improvements such as efficient kernel selection, ARD for feature selection and sparse GP techniques, PoLoN has the potential to handle even larger, more complex datasets while maintaining accurate signal detection and parameter estimation.

## Software and Data Availability

The PoLoN and PoLoN-SB software was written in Python and is available via GitHub at <https://github.com/AnushkaSaha25/PoLoN-Process>.

## Acknowledgments

A.S. and A.V.M. acknowledge financial and logistical support from the Center for Quantitative Biology, Rutgers University. A.G. is supported by the DOE Office of Science, Award No. DE-SC0023524, FermiForward Discovery Group, LLC under Contract No. 89243024CSC000002 with the U.S. Department of Energy, Office of Science. The authors are grateful to the Office of Advanced Research Computing (OARC) at Rutgers University for providing access to the Amarel cluster and associated research computing resources. The authors also acknowledge the work of

the ATLAS Collaboration to record or simulate, reconstruct, and distribute the Open Data used in this paper, and to develop and support the software with which it was analyzed.

---

- [1] ATLAS Collaboration, Observation of a new particle in the search for the Standard Model Higgs boson with the ATLAS detector at the LHC, *Physics Letters B* **716**, 1 (2012).
- [2] CMS Collaboration, Observation of a new boson at a mass of 125 GeV with the CMS experiment at the LHC, *Physics Letters B* **716**, 30 (2012).
- [3] R. F. Egerton and M. Malac, Electron energy-loss spectroscopy in the TEM, *Journal of Electron Spectroscopy and Related Phenomena* **143**, 43 (2005).
- [4] C. Colliex, From early to present and future achievements of EELS in the TEM, *European Physical Journal Applied Physics* **97**, 38 (2022).
- [5] M. A. Isaacs, J. Davies-Jones, P. R. Davies, S. Guan, R. Lee, D. J. Morgan, and R. Palgrave, Advanced XPS characterization: XPS-based multi-technique analyses for comprehensive understanding of functional materials, *Materials Chemistry Frontiers* **5**, 7931 (2021).
- [6] D. N. G. Krishna and J. Philip, Review on surface-characterization applications of X-ray photoelectron spectroscopy (XPS): Recent developments and challenges, *Applied Surface Science Advances* **12**, 100332 (2022).
- [7] P. S. Bagus and H.-J. Freund, X-ray photoelectron spectroscopy as a useful tool to study surfaces and model systems for heterogeneous catalysts: A review and perspective, *Surface Science* **745**, 122471 (2024).
- [8] R. Abbasi *et al.*, Time-integrated searches for point-like sources of neutrinos with the 40-string IceCube detector, *Proceedings of Science (ICRC2010)* **HEP2010**, 1185 (2010).
- [9] R. Abbasi *et al.*, Measurement of the atmospheric muon neutrino energy spectrum from 100 GeV to 400 TeV with IceCube, *Physical Review D* **83**, 012001 (2011).
- [10] M. G. Aartsen *et al.* (IceCube Collaboration), Evidence for high-energy extraterrestrial neutrinos at the IceCube detector, *Science* **342**, 1242856 (2013).
- [11] M. G. Aartsen *et al.*, Observation of high-energy astrophysical neutrinos in three years of IceCube data, *Physical Review Letters* **113**, 101101 (2014).
- [12] W. J. Borucki *et al.*, Kepler planet-detection mission: Introduction and first results, *Science* **327**, 977 (2010).
- [13] G. R. Ricker *et al.*, Transiting exoplanet survey satellite (TESS), *Journal of Astronomical Telescopes, Instruments, and Systems* **1**, 014003 (2015).
- [14] A. Gal-Yam, Observational and physical classification of supernovae, in *Handbook of Supernovae*, edited by A. W. Alsabti and P. Murdin (Springer International Publishing, 2017) pp. 1–43.
- [15] Z. Ivezic *et al.*, LSST: From science drivers to reference design and anticipated data products, *The Astrophysical Journal* **873**, 111 (2019).
- [16] C. Meegan *et al.*, The Fermi gamma-ray burst monitor, *The Astrophysical Journal* **702**, 791 (2009).
- [17] P. A. Evans *et al.*, Methods and results of an automatic analysis of a complete sample of Swift-XRT observations of GRBs, *Monthly Notices of the Royal Astronomical Society* **397**, 1177 (2009).
- [18] J.-L. Starck, F. Murtagh, and A. Bijaoui, *Image Processing and Data Analysis: The Multiscale Approach* (Cambridge University Press, UK, 1998).
- [19] M. Frate, K. Cranmer, S. Kalia, A. Vandenberg-Rodes, and D. Whiteson, Modeling smooth backgrounds and generic localized signals with Gaussian Processes, [arXiv:1709.05681 \[physics.data-an\]](https://arxiv.org/abs/1709.05681) (2017).
- [20] S.-J. Baek, A. Park, Y.-J. Ahn, and J. Choo, Baseline correction using asymmetrically reweighted penalized least squares smoothing, *Analyst* **140**, 250 (2015).
- [21] J. A. Nelder and R. W. M. Wedderburn, Generalized linear models, *Journal of the Royal Statistical Society: Series A* **135**, 370 (1972).
- [22] A. C. Cameron and P. K. Trivedi, *Regression Analysis of Count Data* (Cambridge University Press, UK, 1998).
- [23] M. K. Hutchinson and M. C. Holtman, Analysis of count data using Poisson regression, *Research in Nursing & Health* **28**, 408 (2005).
- [24] G. C. White and R. E. Bennetts, Analysis of frequency count data using the negative binomial distribution, *Ecology* **77**, 2549 (1996).
- [25] P. Mehta, M. Bukov, C.-H. Wang, A. G. R. Day, C. Richardson, C. K. Fisher, and D. J. Schwab, A high-bias, low-variance introduction to Machine Learning for physicists, *Phys. Rep.* **810**, 1 (2019).
- [26] J. W. Rocks and P. Mehta, Memorizing without overfitting: Bias, variance, and interpolation in overparameterized models, *Phys. Rev. Research* **4**, 013201 (2022).
- [27] C. E. Rasmussen and C. K. I. Williams, *Gaussian Processes for Machine Learning* (The MIT Press, Cambridge, MA, 2005).
- [28] C. M. Bishop, *Pattern Recognition and Machine Learning* (Springer, New York, NY, 2006).
- [29] J. P. Cunningham, Z. Ghahramani, and C. E. Rasmussen, Gaussian Processes for time-marked time-series data, *International Conference on Artificial Intelligence and Statistics* **22**, 255 (2012).
- [30] D. Foreman-Mackey, E. Agol, S. Ambikasaran, and R. Angus, Fast and scalable Gaussian Process modeling with applications to astronomical time series, *The Astronomical Journal* **154**, 220 (2017).

- [31] K. G. Iyer, E. Gawiser, S. M. Faber, H. C. Ferguson, J. Kartaltepe, A. M. Koekemoer, C. Pacifici, and R. S. Somerville, Nonparametric star formation history reconstruction with Gaussian Processes. I. Counting major episodes of star formation, *The Astrophysical Journal* **879**, 116 (2019).
- [32] T. A. Gordon, E. Agol, and D. Foreman-Mackey, A fast, two-dimensional Gaussian Process method based on celerite: Applications to transiting exoplanet discovery and characterization, *The Astronomical Journal* **160**, 240 (2020).
- [33] S. Aigrain and D. Foreman-Mackey, Gaussian Process regression for astronomical time series, *Annual Review of Astronomy and Astrophysics* **61**, 329 (2023).
- [34] C. J. Moore, C. P. L. Berry, A. J. K. Chua, and J. R. Gair, Improving gravitational-wave parameter estimation using Gaussian Process regression, *Phys. Rev. D* **93**, 064001 (2016).
- [35] A. Gandrakota, A. Lath, A. V. Morozov, and S. Murthy, Model selection and signal extraction using Gaussian Process regression, *Journal of High Energy Physics* **2023** (2023).
- [36] R. Izsák, Maximum likelihood fitting of the Poisson lognormal distribution, *Environmental and Ecological Statistics* **15**, 143 (2008).
- [37] S. Shaban, Poisson-lognormal distributions, in *Lognormal distributions* (Routledge, 2018).
- [38] K. P. Murphy, *Probabilistic Machine Learning: An introduction* (The MIT Press, Cambridge, MA, 2022).
- [39] S. Akram and Q. U. Ann, Newton Raphson method, *International Journal of Scientific & Engineering Research* **6**, 1748 (2015).
- [40] J. Verbeke and R. Cools, The Newton-Raphson method, *International Journal of Mathematical Education in Science and Technology* **26**, 177 (1995).
- [41] B. P. Sangal and A. K. Biswas, The 3-parameter lognormal distribution and its applications in hydrology, *Water Resources Research* **6**, 505 (1970).
- [42] C. G. Broyden, Quasi-Newton methods and their application to function minimisation, *Mathematics of Computation* **24**, 365 (1970).
- [43] R. Fletcher, A new approach to variable metric algorithms, *The Computer Journal* **13**, 317 (1970).
- [44] D. Goldfarb, A family of variable-metric methods derived by variational means, *Mathematics of Computation* **24**, 23 (1970).
- [45] D. F. Shanno, Conditioning of quasi-Newton methods for function minimization, *Mathematics of Computation* **24**, 647 (1970).
- [46] R. H. Byrd, P. Lu, J. Nocedal, and C. Zhu, A limited memory algorithm for bound constrained optimization, *SIAM Journal on scientific computing* **16**, 1190 (1995).
- [47] S. D. Bass, A. De Roeck, and M. Kado, The Higgs boson implications and prospects for future discoveries, *Nature Reviews Physics* **3**, 608 (2021).
- [48] A. Sopczak, Higgs boson searches at the LHC beyond the Standard Model, *Physics* **6**, 1132 (2024).
- [49] H. Fanaee-T and J. Gama, Event labeling combining ensemble detectors and background knowledge, *Progress in Artificial Intelligence* **2**, 113 (2014).
- [50] ATLAS Collaboration, *Review of the 13 TeV ATLAS Open Data release*, Tech. Rep. (CERN, Geneva, 2020).
- [51] J. M. Hilbe, *Negative Binomial Regression* (Cambridge University Press, UK, 2012).
- [52] D. Duvenaud, J. Lloyd, R. Grosse, J. Tenenbaum, and G. Zoubin, Structure discovery in nonparametric regression through compositional kernel search, in *Proceedings of the 30th International Conference on Machine Learning*, Vol. 28 (2013) pp. 1166–1174.
- [53] A. Wilson and R. Adams, Gaussian Process kernels for pattern discovery and extrapolation, in *Proceedings of the 30th International Conference on Machine Learning*, Vol. 28 (2013) pp. 1067–1075.
- [54] J. Quinonero-Candela and C. E. Rasmussen, A unifying view of sparse approximate Gaussian Process regression, *Journal of Machine Learning Research* **6**, 1939 (2005).
- [55] M. Titsias, Variational learning of inducing variables in sparse Gaussian processes, *Journal of Machine Learning Research* **9**, 567 (2009).
- [56] J. Hensman, N. Fusi, and N. D. Lawrence, Gaussian processes for big data, in *Proceedings of the 29th Conference on Uncertainty in Artificial Intelligence (UAI 2013)* (AUAI Press, 2013) pp. 282–290.

## Supplementary Figures

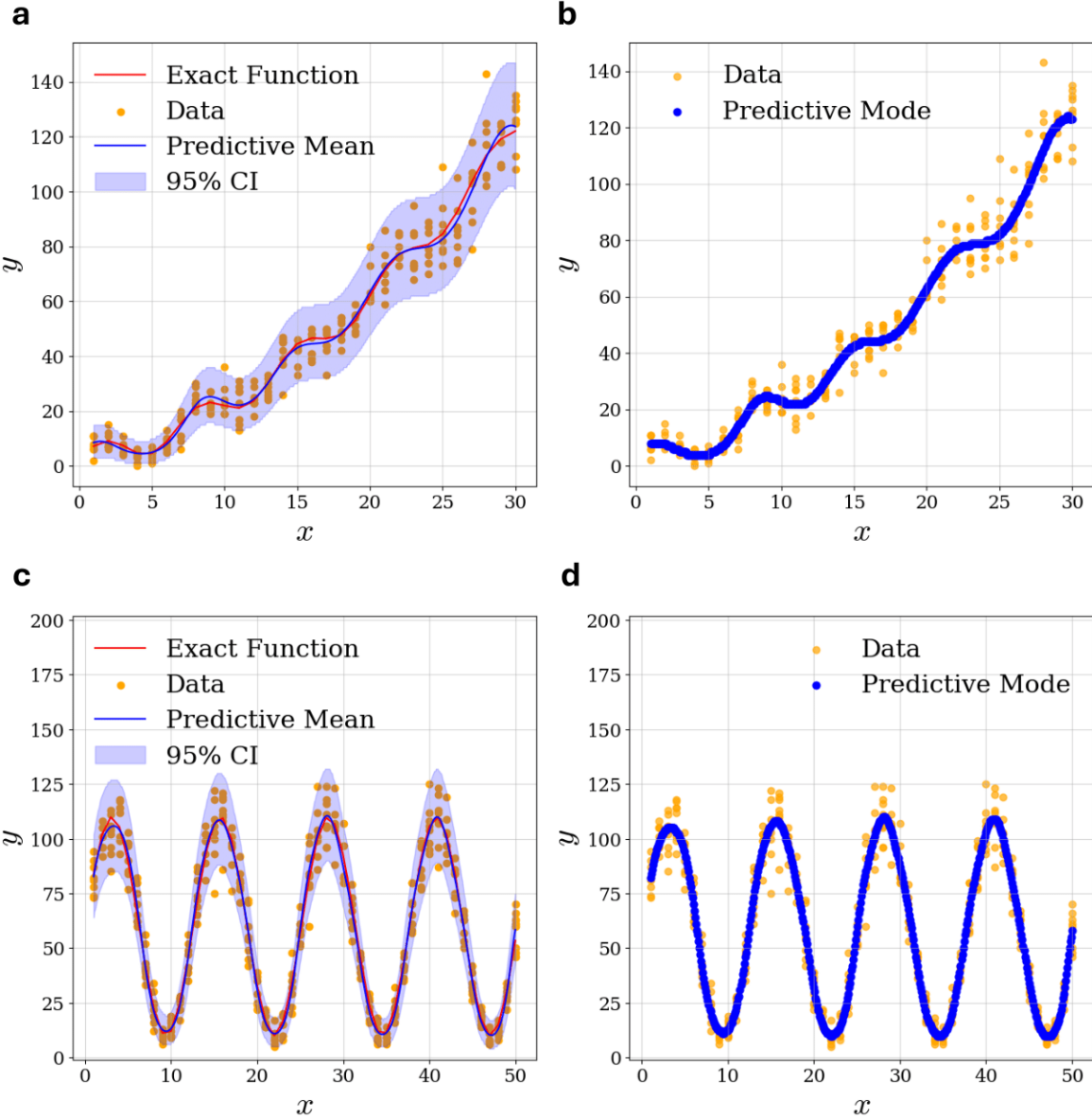
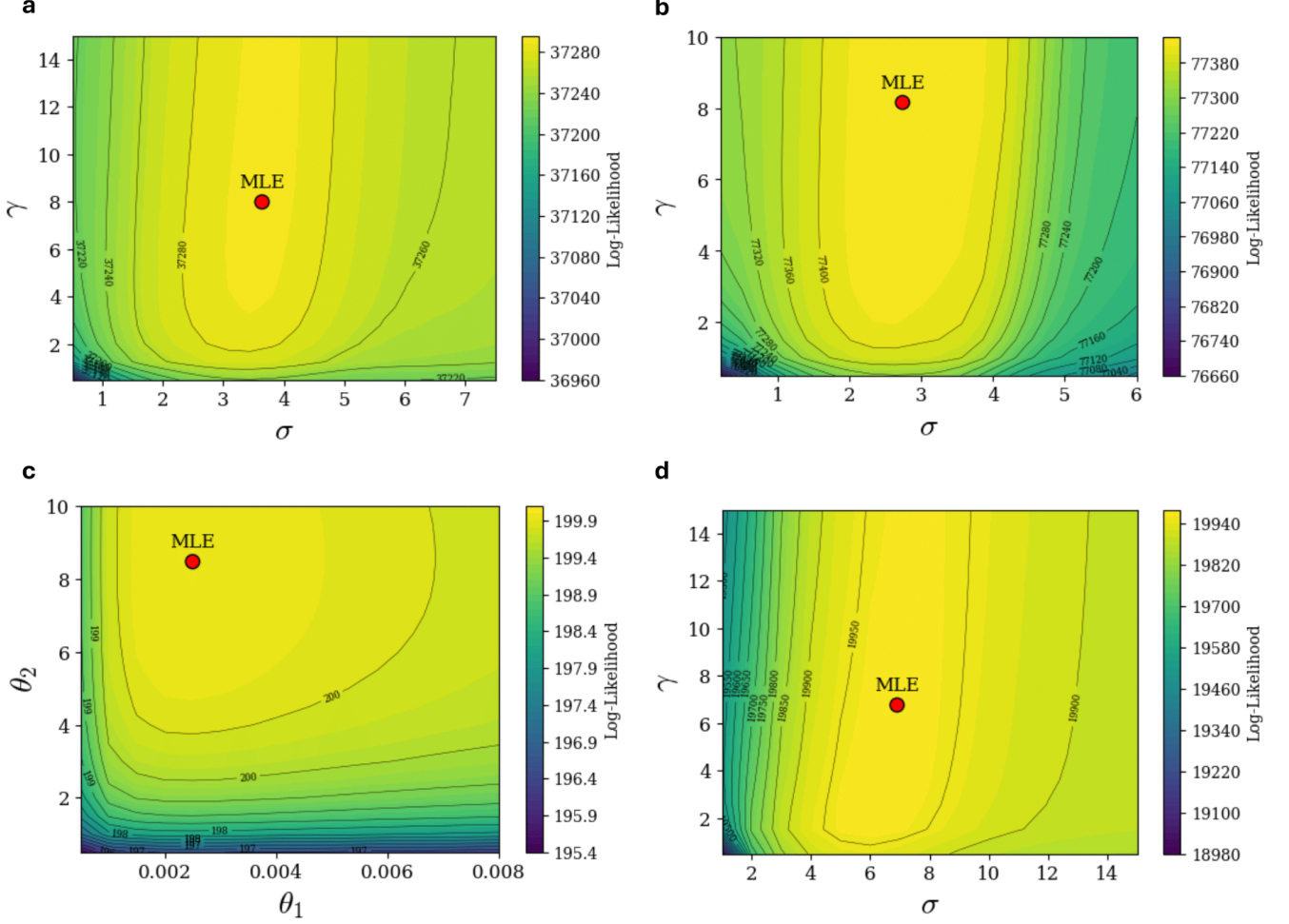


FIG. S1: Additional PoLoN predictions for 1D integer-count data. Panels (a–b): same as Fig. 1a,b but for  $\alpha(x)$  following a quadratic trend with superimposed oscillations (red curve). Panels (c–d): same as Fig. 1a,b but for  $\alpha(x)$  following a purely oscillatory trend (red curve).



**FIG. S2: Kernel hyperparameter optimization: additional posterior log-likelihood landscapes.** Panels (a-c): same as Fig. 2 but for  $\alpha(x)$  characterized by a quadratic trend with superimposed oscillations (Fig. S1a) (a), a purely oscillatory trend (Fig. S1c) (b), and an exponential decay (Fig. 1c) (c). Panel (d) shows the posterior log-likelihood landscape for the 2D exact Poisson rate  $\alpha(x, y)$  characterized by a linear trend in the  $x$  direction with superimposed oscillations in the  $y$  direction. In each panel, the optimized (MLE) hyperparameters are marked with a red dot:  $\sigma^* = 3.635$ ,  $\gamma^* = 8.008$  (a);  $\sigma^* = 2.739$  and  $\gamma^* = 8.173$  (b);  $\theta_1^* = 0.0025$  and  $\theta_2^* = 8.500$  (c);  $\sigma^* = 6.898$  and  $\gamma^* = 6.804$  (d).

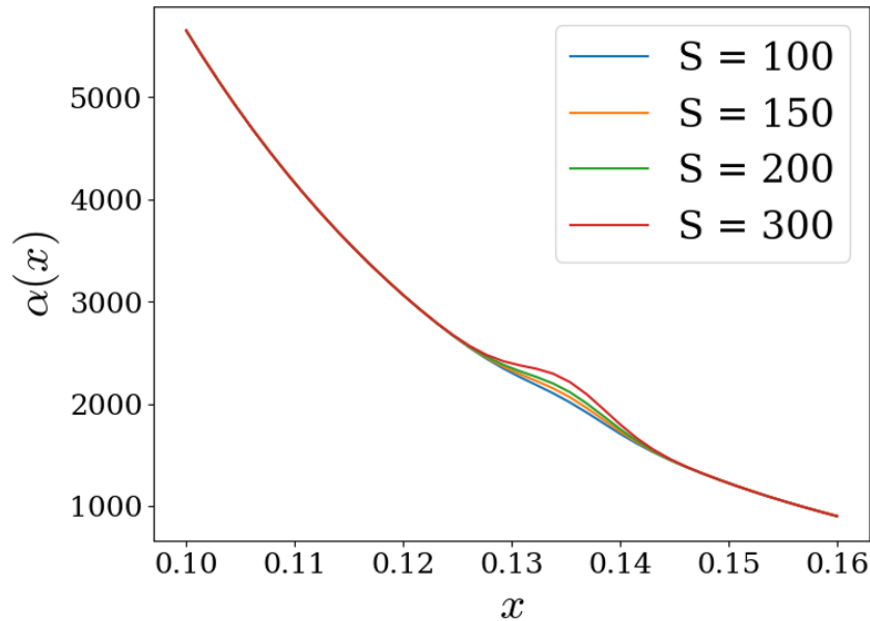


FIG. S3: **Poisson rate functions for separating signal from background in synthetic datasets.**

Representative examples of Poisson rate functions  $\alpha(x)$ , Eq. (46), for the exponentially decaying background with a Gaussian signal of varying strength  $S$ .